IEEE Access
Multidisciplinary | Rapid Review | Open Access Journal

Received 14 June 2024, accepted 19 July 2024, date of publication 29 July 2024, date of current version 20 August 2024.

Digital Object Identifier 10.1109/ACCESS.2024.3434646

RESEARCH ARTICLE

Modeling Partially-Dielectric Unit Cells for OAM Transmitarrays

MIGUEL A. BALMASEDA-MÁRQUEZ[1], GUIDO VALERIO[2,3], PABLO PADILLA[1], ÁNGEL PALOMARES-CABALLERO[4], JUAN F. VALENZUELA-VALDÉS[1], AND CARLOS MOLERO[1], (Member, IEEE)

[1]National Department of Signal Theory, Telematics and Communications, Research Centre for Information and Communication Technologies (CITIC-UGR), University of Granada, 18071 Granada, Spain
[2]CNRS, Laboratoire de Génie Electrique et Electronique de Paris (GeePs), Sorbonne Université, 75252 Paris, France
[3]CentraleSupélec, CNRS, Laboratoire GeePs, Université Paris-Saclay, 91192 Gif-sur-Yvette, France
[4]UMR CNRS 6164, Institut d'Electronique et des Technologies du numéRique (IETR), INSA Rennes, 35700 Rennes, France

Corresponding author: Miguel A. Balmaseda-Márquez (migbalmar@ugr.es)

This work was supported in part by European Union NextGenerationEU/Plan de Recuperación Transferencia y Resiliencia (PRTR) funded by Ministerio de Ciencia, Innovación y Universidades (MICIU)/Agencia Estatal de Investigación (AEI)/10.13039/501100011033 under Grant IJC2020-043599-I; in part by Spanish Government under Project PID2020-112545RB-C54, Project PDC2022-133900-I00, Project PDC2023-145862-I00, Project TED2021-129938B-I00, and Project TED2021-131699B-I00; in part by the Predoctoral Grant FPU21/02219; and in part by European Cooperation in Science and Technology (COST) through the COST Action SyMat under Grant CA18223.

ABSTRACT The presented study introduces a semi-analytical circuit model (CM) to fully characterize a dielectric unit cell structure made by blocks instead of applying the effective medium theory. A fitting strategy is used to a obtain a better understanding of the properties of the unit cell. Then, the approach is used to develop a semi-analytical model, showing a good agreement with the scattering parameters extracted from a full-wave simulator. By tuning the dielectric material, our model can describe the behaviour of unit cells with different permittivities and electrical sizes. Finally, as an application for the analyzed dielectric unit cells, transmitarrays to generate orbital angular momentum (OAM) waves are designed and 3D-printed. The measured results show good performance for different OAM modes at 31 GHz.

INDEX TERMS Circuit models, design equations, dielectric, metamaterial, orbital angular momentum, unit cells.

I. INTRODUCTION

Nowadays fully-dielectric devices have emerged for applications on electromagnetic (EM) waves to design high-gain antennas. However, these devices can be very costly using traditional methods of manufacturing. The development of 3-D printing techniques in dielectric, such as stereolithography (SLA), led to a reduction on the production cost and the achievement of high precision in their manufacturing process [1]. Using this type of technology, dielectric resonator antennas [2], [3], reflectarrays [4], [5], [6], transmitarrays [7], [8] and lenses [9], [10], [11], [12], [13], [14], [15], [16], [17], [18] can be made. Among these structures, transmitarrays (TAs) can be seen as an intermediate solution between phased arrays and high-gain lenses [19], [20], and find applications in satellite communication in different bands [21]. Their advantage is that directive radiation patterns can be produced without the use of a complex and lossy feeding network as it would be needed with a phased arrays [22].

To enable various designs involving a fully-dielectric unit cell, a variable relative permittivity (ε_r) is required. Several works have achieved this permittivity gradient by modifying the ratio between air and dielectric within the unit cell, thereby achieving a gradual transition between the permittivity of air ($\varepsilon_r = 1$) and the desired material [11], [12], [15], [17], [18]. In most of the studies, the final permittivity is calculated using the effective medium theory, which approximates it as a volumetric average between air and dielectric [9], [23]. However, it should be noted that this approach may not be applicable if the unit cell size is not sufficiently small regarding to the wavelength in the homogenized medium.

The associate editor coordinating the review of this manuscript and approving it for publication was Davide Ramaccia.

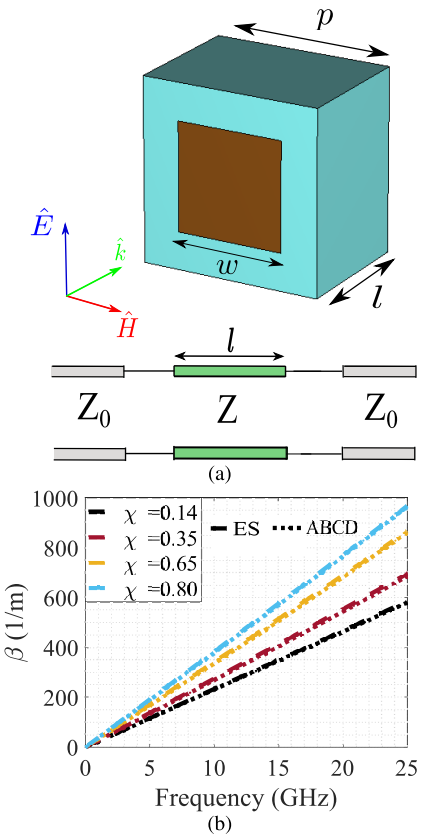

FIGURE 1. (a) Square-shaped unit cell with length l and CM. Blue and brown zones correspond to air and dielectric, respectively. (b) Comparison between ABCD method and eigensolver for several square-shaped dielectric unit cell with ε_r of 5. Structure parameters: $p = 2.7$ mm, $l = 2$ mm.

In this work, we investigate the design and fabrication of transmitarrays based on distributions of square-shaped fully dielectric unit cells, whose size is not necessarily much smaller than the operational wavelength. In fact a weak frequency dispersion of the metasurface helps to obtain a model accurate over a large bandwidth. The analysis consisted of varying the ratio between dielectric and air area by means of simulations via external commercial software. This ratio is called filling factor. The effective permittivity of the unit cell associated with a particular filling factor is computed and assumed to be frequency-independent up to wavelength values similar to the unit cell periodicity. This facilitates a circuit-model conception of the problem, leading to faster calculations and a deeper comprehension of the structure. The range of applicability of the model is examined, assessing the relative error of our model in different situations in order to evaluate the limitations. The circuit approach is finally validated as a design tool in the last section, where a set of transmitarrays emitting Orbital Angular Momentum (OAM) waves are designed, fabricated and experimentally tested with very good performance. This type of arrangement have been selected due to dielectric designs involving OAM generation has proven to be quite robust in different frequency ranges [12], [24], [25].

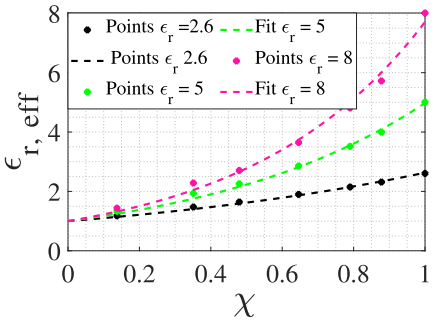

FIGURE 2. Representation of the square-shaped unit cell model, fitting extracted from the calculated results (dotted line) with the simulations for several χ and ε_r. Structure fixed parameters $p = 2.7$ mm.

II. MODELING AND DEFINITION OF THE UNIT CELL

The periodic metamaterial slab of thickness l under study has unit cell defined as a volumetric square-shaped box with dimensions $w \times w \times l$, made of a material with relative permittivity ε_r. It is periodic along the transversal directions x, y with period p, $p \geq w$. A scheme of the unit cell is shown in Fig. 1. Along the z axis this unit cell has finite thickness l and is embedded in air on both sides. Propagation is observed along the z-axis assuming air at both sides of the unit cell. In order to characterize the unit cell, a study about its properties by varying the parameter w for a fixed p is carried out. This implies the modification of the filling factor χ, defined as the ratio between the dielectric surface and the unit cell surface in a transverse cross section of the unit cell:

$$\chi = \frac{w^2}{p^2}. \tag{1}$$

The unit cell is excited by a normally incident plane wave. Several permittivity values will be considered. The model can be homogenized, in the sense that an effective permittivity $\varepsilon_{r,\,\mathrm{eff}}$ can be found for a given filling factor χ. The homogenization hypotheses assumes that a plane wave travelling across the structure goes through the same phase shift due to a dielectric slab of thickness l of a homogeneous material. This reduces the complexity of the analysis and facilitates the use of techniques based on CMs. The computation of the effective-permittivity parameter will be carried out by a closed-form formula, illustrated in Section II-B. Previously, Section II-A describes how this formula is deduced.

A. OBTAINING THE EFFECTIVE PERMITTIVITY

The first step to fully-characterize the unit cell is to calculate $\varepsilon_{r,\,\mathrm{eff}}$ for a given χ. To do this, we first obtain the phase constant β of the fundamental propagating mode inside the unit cell. Two methods have been employed for this purpose. On the one hand, a full-wave electromagnetic simulator is used (CST Microwave Studio) to compute the scattering parameters of the unit cell when a plane wave impinges normally on the metamaterial slab. The scattering parameters

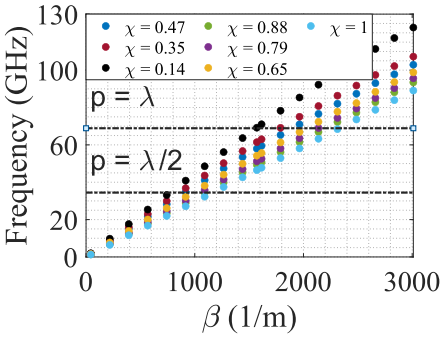

(a)

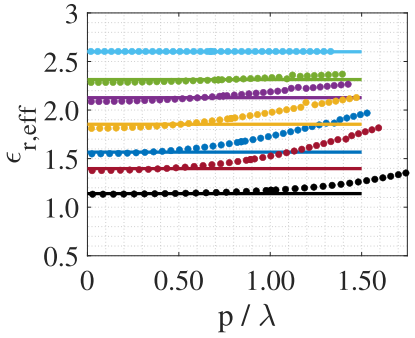

(b)

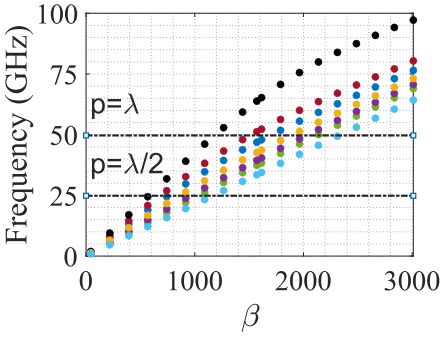

(c)

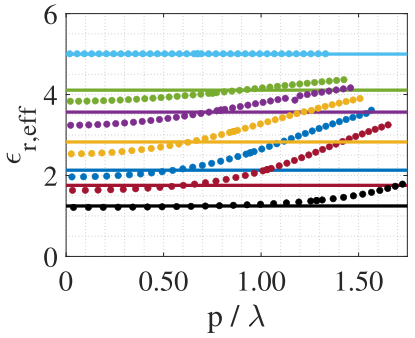

(d)

FIGURE 3. Frequency vs phase constant for several fillings factors. (a) Frequency vs β for $\varepsilon_r = 2.6$ (b) $\varepsilon_{r,\,\mathrm{eff}}$ vs p/λ for $\varepsilon_r = 2.6$ (c) Frequency vs β for $\varepsilon_r = 5$ (d) $\varepsilon_{r,\,\mathrm{eff}}$ vs p/λ for $\varepsilon_r = 5$. The legend is the same for all figures.

are converted to an ABCD formalism, where the propagation constant is calculated by using the following expression [20]:

$$\cos(\beta l) = \frac{A+D}{2}. \tag{2}$$

On the other hand, β can also be estimated using the Eigen-Solver (ES) of CST MicrowaveStudio. It computes the frequency-dependent phase constants of waves propagating inside the dielectric structure by assuming an infinte thickness $l \to +\infty$. The phase constant under interest is the one belonging to the lowest-order or fundamental mode. No additional calculations are needed by this way. Fig. 1(b) shows the evolution of β versus frequency for different filling factors χ (see the caption). The operation wavelength in the dielectric ($\varepsilon_r = 5$) at the highest frequency is $\lambda = 5.3$ mm, corresponding to $p \approx \lambda/2$. λ is calculated as $\lambda = \lambda_0/\sqrt{\varepsilon_r}$, with λ_0 being the wavelength in vacuum. The solution given by both methods coincides in the entire frequency band in all the cases. This confirms that only the fundamental mode computed with the ES is significantly excited at the air-metamaterial interface under plane-wave incidence, and no further reactive contribution is given by the interface. It is important to remark the linear relationship with frequency, which will be important to assume a wideband frequency-independent effective permittivity.

The computation of the effective permittivity in terms of β is carried out through the following expression:

$$\varepsilon_{r,\,\mathrm{eff}} = \left[\frac{\beta c}{2\pi f}\right]^2. \tag{3}$$

Since β is assumed to be linear in frequency (this assumption works well in the frequency region under interest), this implies that $\varepsilon_{r,\,\mathrm{eff}}$ can be assumed frequency independent. The dependence of $\varepsilon_{r,\,\mathrm{eff}}$ with respect to χ is otherwise more complex. The study of this dependence will lead to the deduction of a semi-analytical formula relating both parameters.

B. DEVELOPMENT OF THE SEMI-ANALYTICAL MODEL

In the previous subsection, we presented the methodologies to obtain β and therefore $\varepsilon_{\mathrm{eff}}$. In order to see the behavior of $\varepsilon_{\mathrm{eff}}$ with χ, a most exhaustive analysis of the unit cell will be carried out, by varying the filling factor from $\chi = 0$ (only air) to $\chi = 1$ (only dielectric) for three different values of ε_r.

Fig. 2 depicts three different curves obtained for a single frequency, each associated with a different permittivity value. The dots represent discrete values of $\varepsilon_{\mathrm{eff}}$ obtained by using (3). In all cases, the operation wavelength in the dielectric satisfies $p = \lambda/2$. That is, for $\varepsilon_r = 2, f = 39.3$ GHz; for $\varepsilon_r = 5, f = 25$ GHz; for $\varepsilon_r = 8, f = 19.6$ GHz. A similar evolution of the discrete points with respect χ is appreciated, all of them emulating an exponential tendency. In this sense, it can readily be deduced that the relative effective permittivity $\varepsilon_{r,\mathrm{eff}}$ can be estimated from the following analytical expression

$$\varepsilon_{r,\mathrm{eff}}(\varepsilon_r, \chi) = e^{\chi \log \varepsilon_r}. \tag{4}$$

The curves obtained by using (4) are plotted in dashed lines in Fig. 2. The fitting between the curve and the discrete values is quite good, thus the expression in (4) can be used for a faster calculation of the $\varepsilon_{r,\mathrm{eff}}$. In fact, the CPU time in CST is,

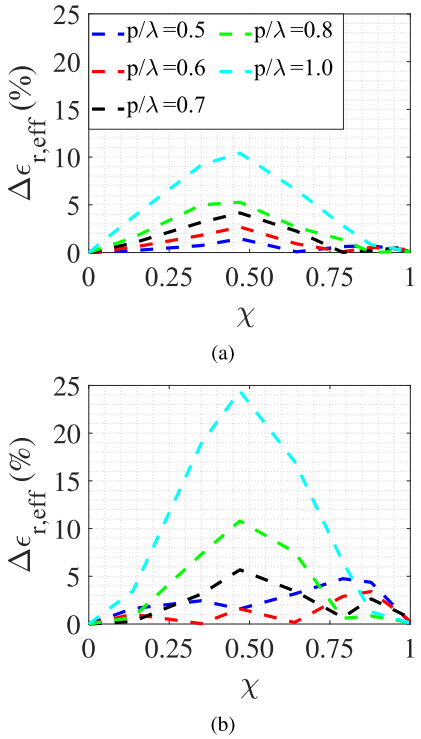

FIGURE 4. Relative error between the theoretical analysis and the simulation results (a) Square-shaped unit cell, $\varepsilon_r = 2.6$ (b) Same case for $\varepsilon_r = 5$.

at least, three orders of magnitude larger than the computation time needed by our approach.

Interestingly, for values of $\varepsilon_r \to 1$ our model (4) reduces to the linear relation $\varepsilon_{eff} = 1 + \chi\,(\varepsilon_r - 1)$ as often used in the literature (e.g. in [9] where this linear model is proposed for different geometries of the periodic lattice and the dielectric embedding).

Once the expression in (4) has been validated, there is not need to use commercial solvers anymore. From this, the propagation constant and characteristic impedance associated with a given $\varepsilon_{r,\,eff}$ are easily obtained by:

$$\beta = \sqrt{\varepsilon_{r,\,eff}}\frac{\omega}{c} \tag{5}$$

$$Z = \eta_0/\sqrt{\varepsilon_{r,\,eff}} \tag{6}$$

Both expressions define a transmission-line model as that in Fig. 1, which will be used below to design and compute the scattering parameters of different unit cell configurations.

III. STUDY OF THE LIMITATIONS OF THE MODEL

In order to gain a better understanding of the limitations of our model, we conducted several studies for two different permittivities, $\varepsilon_r = 2.6$ and $\varepsilon_r = 5$ for different frequency values. We are particularly interested in frequency values for which $p \geq \lambda/2$. Fig. 3 illustrates the behaviour of β over the frequency for $\varepsilon_r = 2.6$. The dotted horizontal lines denote the points where λ matches the periodicity of the unit cell (p) or half the period. The curves exhibit a high degree of linearity, confirming the constant behaviour of the $\varepsilon_{r,eff}$. Additionally, we investigated the behavior of this parameter in relation to the relative periodicity (p/λ), as shown in Fig. 3(b). The horizontal lines represent the theoretical result of $\varepsilon_{r,\,eff}$ computed with (4) while the dotted line represent the results from (3), assumed *exact*. Consequently, the same studies were performed for $\varepsilon_r = 5$ as can be seen in Fig. 3(c) and Fig. 3(d). Notably, a close match is observed for low and very high χ values, with the largest discrepancy occurring at intermediate values.

To further analyze this discrepancy, we examine the relative error in Fig. 4(a) and Fig. 4(b). These figures depict the relative error, calculated as the percentage difference between the analytical formula in (4) and simulation results from (3), for various filling factors ranging from 0 to 1. In the case of $\varepsilon_r = 2.6$, the error curve remains below 5% for the majority of cases. However, at $p/\lambda = 1$, the relative error increases to approximately 11% for intermediate values of χ. Similarly, For $\varepsilon_r = 5$, the average error stays below 11% except for $p/\lambda = 1$, where it is close to 25%. In any case, even the largest deviations in the calculation of the effective permittivity are compatible with the design proposed in the following section.

It is also worth remarking that an additional restriction may appear due to the excitation of higher-order harmonics in the dielectric region. The cutoff frequency depends on χ. The case with smallest cutoff frequency is that with $\chi = 1$, where the dielectric takes the unit cell dimensions and higher-order harmonics excites for $p = \lambda$. As χ decreases, the cutoff frequency moves towards higher frequencies, and there is no restriction at $p = \lambda$. The highest cutoff frequency is given when $\chi = 0$, setting the limit at $p = \lambda\sqrt{\varepsilon_r} = \lambda_0$.

A. COMPARISON WITH PREVIOUS MODELS

In order to evaluate the robustness of our method, a comparison with the effective medium theory is made for two different values of the wavelength. In fact, we have selected wavelength values $p \geq \lambda/2$, concretely $p = \lambda/2$ and $p = 3\lambda/4$.

The effective medium theory is a linear approach that is supposed to have a range of validity up to cells larger than $\lambda/2$. The formula here presented is otherwise not linear, described by an exponential expression with range of validity beyond $\lambda/2$. To validate this assumption we first consider the permittivity formula employed in the effective-medium theory (reported, for example, in [9]).

$$\varepsilon_P = \varepsilon_r(1-\alpha) + \alpha \tag{7}$$

with α being the volumetric filling factor. This definition of filling factor in terms of volume provides a ε_P identical as if we rather use the surface definition used in his work χ. This is due to the fact that the length of the dielectric block (along the z direction) coincides with the length of the whole unit cell. It is important to remark that in the case of α, the surrounding media is dielectric, being the holes of air the principal media, thus making the definition of α just the

TABLE 1. Comparison table for the different methods to obtain the effective permittivity for $p = \lambda/2$.

	$\varepsilon_r = 2.6$ // $\chi = 0.87$	$\varepsilon_r = 2.6$ // $\chi = 0.137$	$\varepsilon_r = 2.6$ // $\chi = 0.47$	$\varepsilon_r = 5$ // $\chi = 0.87$	$\varepsilon_r = 5$ // $\chi = 0.137$	$\varepsilon_r = 5$ // $\chi = 0.47$
$\varepsilon_{r,\,eff}$	2.31 (<1%)	1.14 (<1%)	1.57 (<1%)	4.11 (5%)	1.35 (10%)	2.13 (2%)
ε_p	2.39 (3.9%)	1.22 (7%)	1.75 (10%)	4.48 (14%)	1.55 (26%)	2.88 (37%)
$\varepsilon_{E\text{-}S}$ $(\lambda/2)$	2.30	1.14	1.59	3.92	1.23	2.10

TABLE 2. Comparison table for the different methods to obtain the effective permittivity for $p = 3\lambda/4$.

	$\varepsilon_r = 2.6$ // $\chi = 0.87$	$\varepsilon_r = 2.6$ // $\chi = 0.137$	$\varepsilon_r = 2.6$ // $\chi = 0.47$	$\varepsilon_r = 5$ // $\chi = 0.87$	$\varepsilon_r = 5$ // $\chi = 0.137$	$\varepsilon_r = 5$ // $\chi = 0.47$
$\varepsilon_{r,\,eff}$	2.31 (<1%)	1.14 (<1%)	1.57 (4%)	4.11 (2%)	1.35 (8%)	2.13 (7%)
ε_p	2.39 (3.5%)	1.22 (6%)	1.75 (7%)	4.48 (11%)	1.55 (24%)	2.88 (25%)
$\varepsilon_{E\text{-}S}$ $(3\lambda/4)$	2.31	1.15	1.64	4.03	1.25	2.30

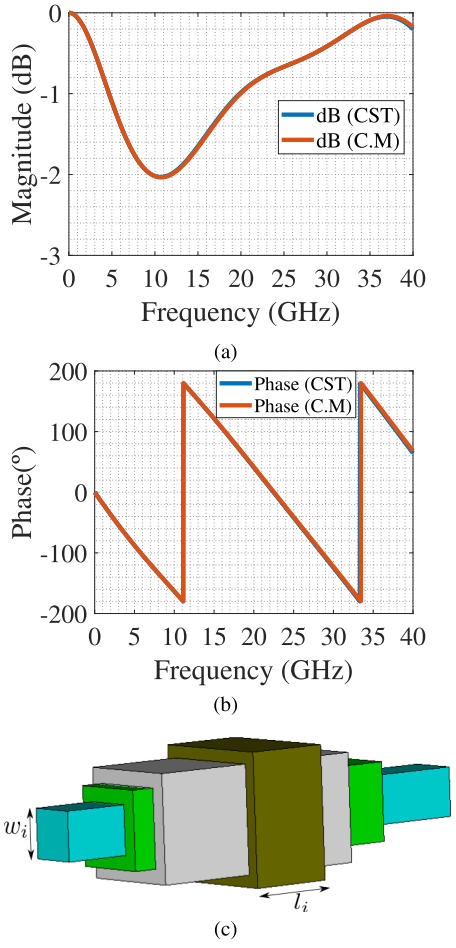

FIGURE 5. Scattering parameters for the cascade of several squared unit cells changing the permittivies and geometry of each unit cell. (a) Transmission coefficient in dB. (b) Transmission coefficient in phase. (c) View of the concatenated unit cells.

opposite as our case (χ) where our surrounding media is air and the principal media is the dielectric. Thus, making the proper change, (7) can be expressed in terms of our definition of filling factor χ as

$$\varepsilon_P = (1 - \chi) + \chi \varepsilon_r \,. \tag{8}$$

The effective permittivity values computed by Eq.(8) will be compared to those from our formula ($\varepsilon_{r,eff}$) and to those computed with the Eigenmode Solver of CST - Studio ($\varepsilon_{E\text{-}S}$) (this last assumed as the exact one). The comparison will be made in terms of the relative error.

Table 1 and table 2 shows the results of an exhaustive comparison for the 2 different values of the wavelength λ remarked at the beginning of this section. In addition, 2 different permittivity values ($\varepsilon_r = 2.6, 5$) are considered. As can be checked in the tables, the deviation manifested when the effective medium theory is applied ((8)) is larger in comparison to our model. The maximum deviation in our model with respect the results given by CST is about 10% in the case involving $\chi = 0.137$ and $\varepsilon_r = 5$. The formula in (8) deviates up to 37% in some cases, such as that regarding $\varepsilon_r = 5$, $\chi = 0.47$. Our model notably improves the predictions for the wavelength values under consideration, where $p \leq \lambda/2$.

B. LIMITATIONS ON THE PERMITTIVITY VALUES

As will be shown, the model can still be used for design purposes, even in the most critical scenarios. It is actually conceived to compute the scattering parameters of unit cells formed by dielectric sections (single or cascaded). And it can be corroborated that deviations of the order of 10-20 % in the effective-permittivity computation are not really dramatic when the scattering parameters of a given unit cell are inspected. For instance, Fig. 5(a)-5(b) illustrate the evolution of the magnitude/phase of the transmission coefficient for the unit cell sketched in Fig. 5(c). The unit cell is a symmetric design formed by 7 dielectric sections. Each section is defined by a particular set involving a permittivity value and a filling factor. The structure parameters are summarized in Table 3 and 4. The agreement between results provided by the circuit model and CST is excellent along the whole band, both in magnitude and phase. Notice that the highest frequency considered is 40 GHz. The highest permittivity taking place in the system is $\varepsilon_r = 6$, with $\chi = 1$, thus the excitation of a higher-order harmonic in this block would start at 45.3 GHz. This effect is not taken into account by our circuit but it still fits very well with CST. This fact corroborates the

TABLE 3. Parameters for the simulation studying the limitation on the permittivity.

Parameters	
w_1 = 1.4mm	l_1 = 1mm
w_2 = 0.5mm	l_2 = 1.6mm
w_3 = 2.1mm	l_3 = 2.2mm
w_4 = 1.72mm	l_4 = 2.7mm
w_5 = 0.9mm	l_5 = 2.2mm
w_6 = 1.1mm	l_6 = 1.6mm
w_7 = 2.0mm	l_7 = 1mm

TABLE 4. Permittivies and filling factors for the simulation studying the limitation on the permittivity.

Permittivities (ε_r)			
ε_1 = 1.5 (blue)	ε_2 = 3.0 (green)	ε_3 = 2.1 (white)	ε_4 = 6.0 (brown)
Filling factors (χ)			
χ_1 = 0.14	χ_2 = 0.35	χ_3 = 0.66	χ_4 = 1

robustness of the model for relatively high frequencies even for non-negligible deviations of the permittivity.

IV. STUDY OF THE IMPACT OF HAVING LOSSY MATERIALS

Finally, further studies considering dielectric losses has been performed, demonstrating that the model works well up to loss tangents of $\tan(d) = 0.05 - 0.1$. The model is therefore robust to account for dielectric with common dielectric losses. To evaluate the robustness of the method when utilizing arbitrary filling factors, we assemble consecutive blocks to create a new unit cell as that in Fig. 6. Each of the blocks, defined by their own w_i and l_i, will have an individual filling factor χ_i. Their corresponding effective permittivity is calculated by using the formula in (4). Fig. 6 also shows the equivalent circuit associated with the unit cell, where each of the blocks is actually represented by a different transmission line section with impedance Z_i, obtained via (6). This model is very useful for a quick design, since the higher number of blocks, the higher CPU time is required in CST. Though the case in Fig. 6 considers the same permittivity in all the blocks, it can be demonstrated that the model keeps robust even for blocks with different permittivities and filling factors.

To see the influence of the dielectric material losses, this unit cell has been simulated. This example is paradigmatic since the structure is long and the influence of the losses can be better appreciated.

A first case already considers a non-negligible value of the loss tangent, $\tan(d) = 0.02$. This value has been introduced in the simulation in CST-Studio. The corresponding transmission coefficient and phase, represented versus frequency, are plotted in Fig.6(b)-6(c). The results associated with the circuit model accounts for the lossless case (they fit well with those provided by CST as shown in Fig. 5 of the main manuscript). It is straightforward to realize that the behavior of the phase does not vary with the inclusion of the losses. Slight modifications can otherwise be appreciated in the magnitude

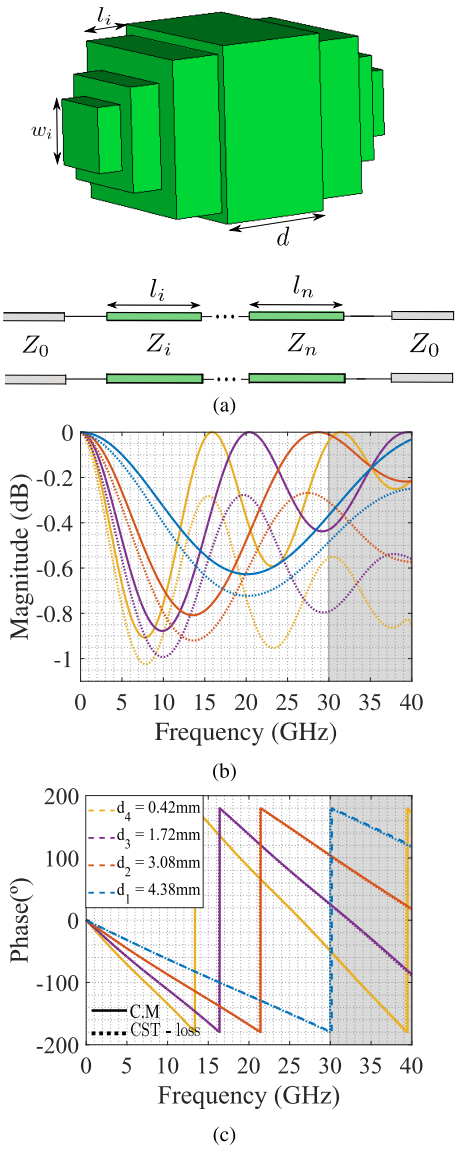

FIGURE 6. (a) A unit cell with seven sections; $w_1 = w_7 = 0.4$ mm, $w_2 = w_6 = 0.5$ mm, $w_3 = w_5 = 0.8$ mm, $w_4 = 2.7$ mm, $l_1 = l_7 = 1$ mm, $l_2 = l_6 = 1.6$ mm, $l_3 = l_5 = 2.4$ mm, $l_4 = 2.7$ mm, d is the parameter to modify. Equivalent CM parameters: $Z_1 = Z_7 = 315.85\ \Omega$, $Z_2 = Z_6 = 284.04\ \Omega$, $Z_3 = Z_5 = 246.54\ \Omega$, $Z_4 = 233.80\ \Omega$, $\varepsilon_r = 2.6$. Scattering parameters for the cascade of several unit cells when there are material losses (b) Magnitude of the transmission coefficient in dB (c) Phase of the transmission coefficient.

of the transmission coefficient. However the magnitude level does not crosses the -1 dB threshold, as in the lossless case.

An additional analysis has been implemented considering larger dielectric losses. Now a extreme case is regarded. In Fig.7(a) -7(b) simulations in CST have been performed for a $\tan(d) = 0.2$. It can be stated that the phase shift between different phase states continues to be stable as if we had no loss at all. The agreement with results from the circuit model corroborates this. However the magnitude level begins to deteriorate, especially for higher frequencies. In any case, this loss tangent is quite big in comparison with most of dielectric materials employed in in radio-frequency devices.

So we can conclude in this aspect that our formulation will be still valid. On the one hand, no modification of the phase behavior is manifested. On the other hand, the impact on the transmission coefficient is substantial when the loss tangent is excessively large.

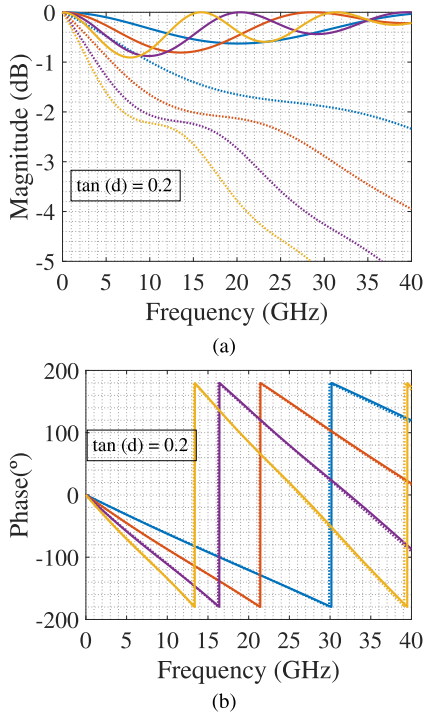

FIGURE 7. Scattering parameters for the cascade of several squared unit cells when there are material losses (a) Magnitude of the transmission coefficient in dB for tan(d) = 0.2 (b) Phase of the transmission coefficient for tan(d) = 0.2.

V. APPLICATION FOR OAM WAVES

The unit cell presented in the previous section will be used for the design of a 2-bits fully-dielectric TA generating orbital angular momentum (OAM) waves [26] in the Ka-band (between 30 − 40 GHz). For the sake of simplicity no dielectric losses are considered for the design. The TA will be formed by a 2-dimensional distribution of unit cells as that in Fig. 6. Each of the cells is tuned to provide a particular phase value. In fact, the term 2-bits indicates that the phases in the unit cells will be discretized to 4 values. Thus 4 phase states differing 90^o are needed. This introduces limitations in gain but simplifies the design process. The tuning of the phase is governed by d which is sketched in Fig. 6.

In order to first validate the model, the scattering parameters of several unit cell configurations have been obtained by CST and our CM, and have been plotted in Fig. 8(a)-(c). The frequency band of interest for the design is highlighted in grey. An excellent agreement between results from CST and the circuit is appreciated in all the frequency span. This design has been chosen due to an improvement in the bandwidth response of the phase thanks to the seven consecutive sections. As can be appreciated in

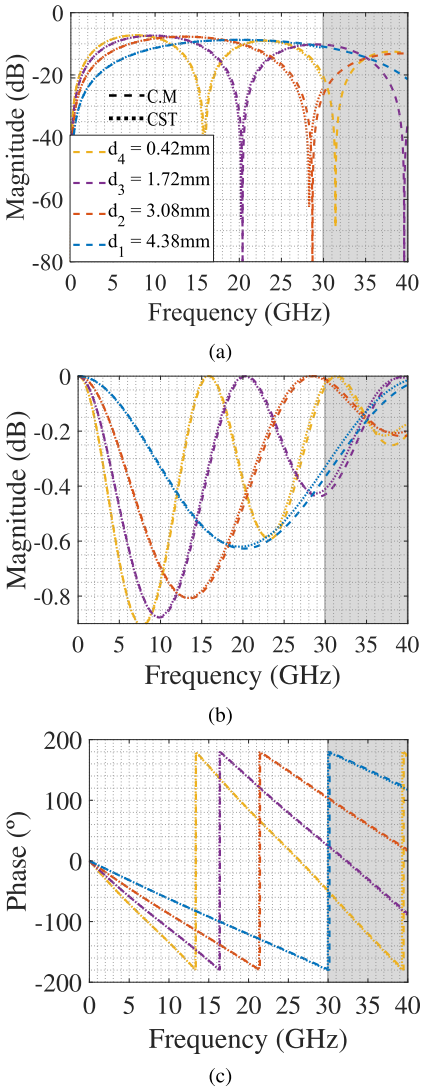

FIGURE 8. Scattering parameters for the cascade of several dielectric blocks (a) Magnitude of the reflection coefficient. (b) Magnitude and (c) Phase of the transmission coefficient.

Fig. 8(b)-(c), the transmission coefficient never crosses the −1 dB threshold and the phases differ in 90^o in the desired band.

The TA will be formed by 40×40 unit cells with periodicity $p = 2.7$ mm. The permittivity will be identical in all the blocks for fabrication constraints ($\varepsilon_r = 2.6$). The phase required for each unit cell in the TA, based on a spherical wave hitting the structure, is determined by Eq. (2) in [27]. After determining the different states of the unit cell, several TAs for OAM generation are designed, spanning from a topological charge of $L = -1, -4, -6$ to $L = 1, 4, 6$, what makes a total of six different TAs. These TAs are fabricated in our facilities using SLA and a resin with a permittivity of $\varepsilon_r = 2.6$.

Once the printing process is completed, the vortex patterns of all TAs are measured. These TAs are designed for a frequency of 31 GHz, ensuring that the phase shift for

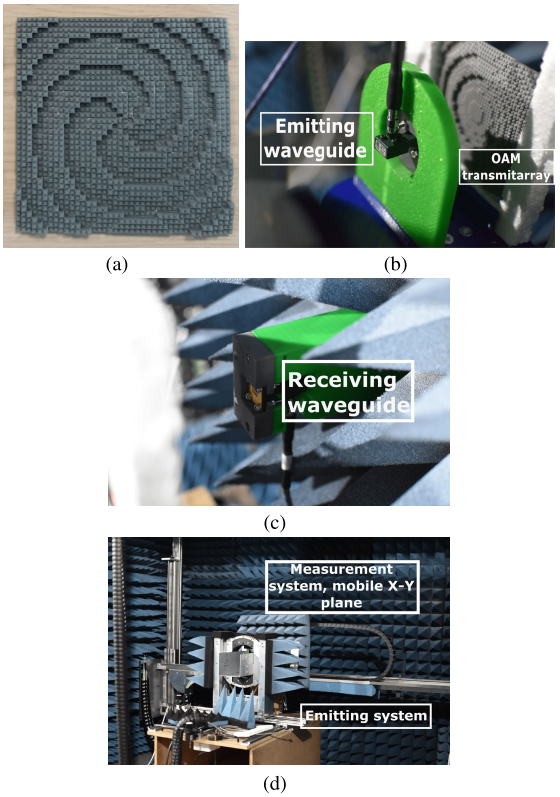

FIGURE 9. Measurement setup includes: (a) L=-4 OAM TAs, (b) Emitting setup with waveguide and OAM TA, (c) Receiving waveguide within shielding, (d) Full setup with XY-motorized acquisition system.

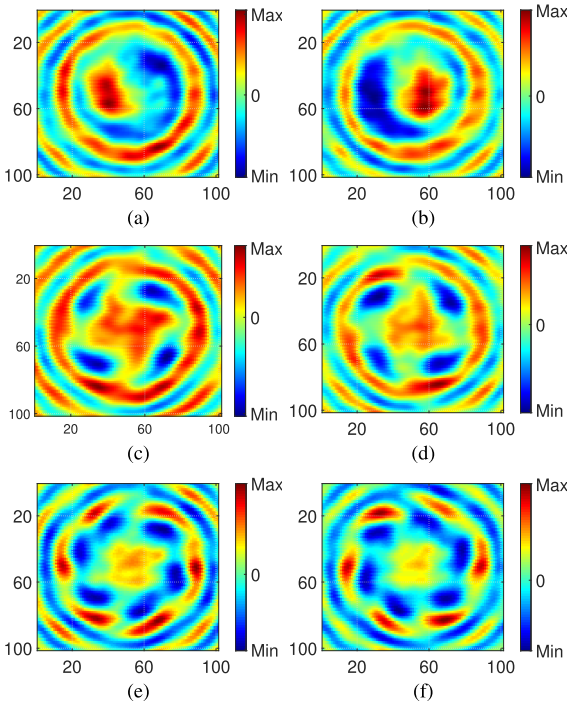

FIGURE 10. Measured E-field for several OAM modes using the fabricated OAM TAs. (a) $L = -1$ (b) $L = 1$ (c) $L = -4$ (d) $L = 4$ (e) $L = -6$ (f) $L = 6$.

each state satisfies the condition of linearity, as depicted in Fig. 8(c). An experimental prototype of TA with $L = 4$ is shown in Fig. 9(a). To measure the vortex pattern, an initial setup is established, as illustrated in Fig. 9(b). A waveguide (WR-34) functioning as a probe is positioned in an XY plane and is moved to capture the entire power of the mode, as can be seen in Fig. 9(c), enabling a comprehensive characterization of the vortex. The setup with the additional waveguide can be observed in Fig. 9(d).

Near-field techniques has been done to measure the scene which was a 30×30 cm^2 square with a 1.5 mm pixel (about 0.5λ of electrical length) size can be seen in Fig. 10-(f) which represents the real part of the electric fields. These type of representations have been selected due to its easily-recognize OAM patterns. These results exhibit the typical characteristics of the OAMs vortexes, in this case we can see as many high intensity and low intensity arms as the number of the mode [26], [28]. Note that the design of each cell has been done via (4), which has some error estimation for intermediate χ. The experimental results validate the predictions.

VI. CONCLUSION

This study focuses on characterizing the unit cell of a periodic fully dielectric metasurface. A circuital model is employed to design OAM transmitarrays. The circuit model elements are calculated in terms of an effective permittivity which is extracted from a semi-analytical formula. Thanks to the use of this formula, the use of commercial software is not necessary. The formula, and therefore the model, provides accurate results up to wavelengths close to the periodicity of the unit cell. Moreover, a comprehensive study on the limitations and the effect of materials losses is made. Then, several transmitarray designs are measured, successfully generating the corresponding OAM modes. The model shows better performance that the effective-medium theory, especially at higher frequencies, and guarantees a quick obtaining of the results, being some order of magnitude faster than CST.

REFERENCES

[1] J. Huang, Q. Qin, and J. Wang, "A review of stereolithography: Processes and systems," *Processes*, vol. 8, no. 9, p. 1138, Sep. 2020. [Online]. Available: https://www.mdpi.com/2227-9717/8/9/1138

[2] M. H. Neshati and Z. Wu, "The determination of the resonance frequency of the TE111y mode in a rectangular dielectric resonator for antenna application," in *Proc. 11th Int. Conf. Antennas Propag.*, vol. 1, Feb. 2001, pp. 53–56.

[3] Y.-L. Li and K.-M. Luk, "A low-cost 3-D printed THz open resonator antenna," *IEEE Antennas Wireless Propag. Lett.*, vol. 22, pp. 84–88, 2023.

[4] N. V. Langhnoja and V. V. Dwivedi, "Comparison of dielectric materials using unit-cell design approach of microstrip reflectarray antenna," in *Proc. Int. Conf. Comput., Commun. Electron. (Comptelix)*, Jul. 2017, pp. 370–372.

[5] Y. He, Z. Gao, D. Jia, W. Zhang, B. Du, and Z. N. Chen, "Dielectric metamaterial-based impedance-matched elements for broadband reflectarray," *IEEE Trans. Antennas Propag.*, vol. 65, no. 12, pp. 7019–7028, Dec. 2017.

[6] P. Mei, S. Zhang, and G. F. Pedersen, "A wideband 3-D printed reflectarray antenna with mechanically reconfigurable polarization," *IEEE Antennas Wireless Propag. Lett.*, vol. 19, pp. 1798–1802, 2020.

[7] A. Massaccesi, P. Pirinoli, V. Bertana, G. Scordo, S. L. Marasso, M. Cocuzza, and G. Dassano, "3D-printable dielectric transmitarray with enhanced bandwidth at millimeter-waves," *IEEE Access*, vol. 6, pp. 46407–46418, 2018.

[8] X. Liu, L. Peng, Y.-F. Liu, W.-S. Yu, Q.-X. Zhao, X. Jiang, S.-M. Li, and C. Ruan, "Ultrabroadband all-dielectric transmitarray designing based on genetic algorithm optimization and 3-D print technology," *IEEE Trans. Antennas Propag.*, vol. 69, no. 4, pp. 2003–2012, Apr. 2021.

[9] A. Petosa and A. Ittipiboon, "A Fresnel lens designed using a perforated dielectric," in *Proc. 9th Int. Symp. Antenna Technol. Appl. Electromagn.*, Jul. 2002, pp. 1–4.

[10] M. Imbert, A. Papió, F. De Flaviis, L. Jofre, and J. Romeu, "Design and performance evaluation of a dielectric flat lens antenna for millimeter-wave applications," *IEEE Antennas Wireless Propag. Lett.*, vol. 14, pp. 342–345, 2015.

[11] J. M. Poyanco, F. Pizarro, and E. Rajo-Iglesias, "Wideband hyperbolic flat lens in the Ka-band based on 3D-printing and transformation optics," *Appl. Phys. Lett.*, vol. 118, no. 12, Mar. 2021, Art. no. 123503, doi: 10.1063/5.0045862.

[12] S. Zhang, R. K. Arya, W. G. Whittow, D. Cadman, R. Mittra, and J. C. Vardaxoglou, "Ultra-wideband flat metamaterial GRIN lenses assisted with additive manufacturing technique," *IEEE Trans. Antennas Propag.*, vol. 69, no. 7, pp. 3788–3799, Jul. 2021.

[13] S. Moreno-Rodríguez, M. A. Balmaseda-Márquez, J. Carmona-Murillo, and Á. Palomares-Caballero, "Polarization-insensitive unit cells for a cost-effective design of a 3-D-printed Fresnel-lens antenna," *Electronics*, vol. 11, no. 3, p. 338, Jan. 2022. [Online]. Available: https://www.mdpi.com/2079-9292/11/3/338

[14] S. Zhang, P. Liu, and W. Whittow, "Design and fabrication of 3-D-printed high-gain broadband Fresnel zone lens using hybrid groove-perforation method for millimeter-wave applications," *IEEE Antennas Wireless Propag. Lett.*, vol. 21, no. 1, pp. 34–38, Jan. 2022.

[15] S. Zhang, R. K. Arya, S. Pandey, Y. Vardaxoglou, W. Whittow, and R. Mittra, "3D-printed planar graded index lenses," *IET Microw., Antennas Propag.*, vol. 10, no. 13, pp. 1411–1419, Oct. 2016.

[16] S. Zhang, "Design and fabrication of 3D-printed planar Fresnel zone plate lens," *Electron. Lett.*, vol. 52, no. 10, pp. 833–835, May 2016. [Online]. Available: https://ietresearch.onlinelibrary.wiley.com/doi/abs/10.1049/el.2016.0736

[17] O. Bjorkqvist, O. Zetterstrom, and O. Quevedo-Teruel, "Additive manufactured dielectric Gutman lens," *Electron. Lett.*, vol. 55, no. 25, pp. 1318–1320, Dec. 2019. [Online]. Available: https://ietresearch.onlinelibrary.wiley.com/doi/abs/10.1049/el.2019.2483

[18] J. M. Monkevich and G. P. Le Sage, "Design and fabrication of a custom-dielectric Fresnel multi-zone plate lens antenna using additive manufacturing techniques," *IEEE Access*, vol. 7, pp. 61452–61460, 2019.

[19] J. Huang, "Microstrip reflectarray," in *Proc. Antennas Propag. Soc. Symp. Dig.*, Jun. 1991, pp. 612–615.

[20] D. M. Pozar, S. D. Targonski, and H. D. Syrigos, "Design of millimeter wave microstrip reflectarrays," *IEEE Trans. Antennas Propag.*, vol. 45, no. 2, pp. 287–296, Feb. 1997.

[21] S. Zainud-Deen, S. M. Gaber, Ha. Malhat, and K. H. Awadalla, "B2. Single feed dual-polarization dual-band transmitarray for satellite applications," in *Proc. 30th Nat. Radio Sci. Conf. (NRSC)*, Apr. 2013, pp. 27–34.

[22] M. Keller, J. Shaker, A. Petosa, A. Ittipiboon, M. Cuhaci, and Y. Antar, "A Ka-band dielectric resonator antenna reflectarray," in *Proc. 30th Eur. Microw. Conf.*, 2000, pp. 1–4.

[23] J. S. Colburn and Y. Rahmat-Samii, "Patch antennas on externally perforated high dielectric constant substrates," *IEEE Trans. Antennas Propag.*, vol. 47, no. 12, pp. 1785–1794, Dec. 1999.

[24] G.-B. Wu, K. F. Chan, S.-W. Qu, K. F. Tong, and C. H. Chan, "Orbital angular momentum (OAM) mode-reconfigurable discrete dielectric lens operating at 300 GHz," *IEEE Trans. THz Sci. Technol.*, vol. 10, no. 5, pp. 480–489, Sep. 2020.

[25] G.-B. Wu, K. F. Chan, K. M. Shum, and C. H. Chan, "Millimeter-wave and terahertz OAM discrete-lens antennas for 5G and beyond," *IEEE Commun. Mag.*, vol. 60, no. 1, pp. 34–39, Jan. 2022.

[26] J. Han, L. Li, H. Yi, and Y. Shi, "1-bit digital orbital angular momentum vortex beam generator based on a coding reflective metasurface," *Opt. Mater. Exp.*, vol. 8, no. 11, p. 3470, Oct. 2018.

[27] S. Yu, L. Li, G. Shi, C. Zhu, X. Zhou, and Y. Shi, "Design, fabrication, and measurement of reflective metasurface for orbital angular momentum vortex wave in radio frequency domain," *Appl. Phys. Lett.*, vol. 108, no. 12, Mar. 2016, Art. no. 121903, doi: 10.1063/1.4944789.

[28] K. Zhang, Y. Wang, Y. Yuan, and S. N. Burokur, "A review of orbital angular momentum vortex beams generation: From traditional methods to metasurfaces," *Appl. Sci.*, vol. 10, no. 3, p. 1015, Feb. 2020. [Online]. Available: https://www.mdpi.com/2076-3417/10/3/1015

MIGUEL A. BALMASEDA-MÁRQUEZ received the B.Sc. degree in physics and the B.Sc. degree in materials engineering from the University of Seville (US), in 2020, and the M.Sc. degree in radiation physics from the University of Granada (UGR), in 2022, where he is currently pursuing the Ph.D. degree. Since 2021, he has been with the National Department of Signal Theory, Telematics and Communications, Research Centre for Information and Communication Technologies (CITIC-UGR). His current research interests include metamaterials, orbital angular momentum waves, and applied electromagnetism.

GUIDO VALERIO received the M.S. degree (cum laude) in electronic engineering and the Ph.D. degree in electromagnetics from the Sapienza University of Rome, Rome, Italy, in 2005 and 2009, respectively.

From February 2008 to August 2008, he was a Visiting Scholar with the University of Houston, Houston, TX, USA. From 2011 to 2014, he was a Researcher with the Institute d'Electronique et de Telecommunications de Rennes (IETR), Rennes, France. Since September 2014, he has been with Sorbonne Université, Paris, France, where he is currently a Professor with the Laboratoire de Génie Electrique et Electronique de Paris. He was the co-author of the Best Papers in Electromagnetic and Antenna Theory at European Conference on Antennas and Propagation, in 2018 and 2020, and the Best Student Paper Award at the 16th European Conference on Antennas and Propagation, in 2022. He was a recipient of the "Leopold B. Felsen Award for Excellence in Electrodynamics," in 2008; the "Barzilai Prize" for the Best Paper at the National Italian Congress of Electromagnetism (XVIII RiNEm), in 2010; and the RMTG Award for Junior Researchers Presented at the IEEE Antennas and Propagation Society Symposium, Memphis, TN, USA, in 2014.

PABLO PADILLA was born in Jaen, Spain, in 1982. He received the Telecommunication Engineering and Ph.D. degrees from the Radiation Group, Signal, Systems and Radiocommunications Department, Technical University of Madrid (UPM), Spain, in 2005 and 2009, respectively. In 2007, he was with the Laboratory of Electromagnetics and Acoustics, École Polytechnique Fédérale de Lausanne, Switzerland, as an invited Ph.D. Student. In 2009, he carried out a post-doctoral position with Helsinki University of Technology (AALTO-TKK). In 2009, he was an Assistant Professor with the Signal Theory, Telematics and Communications Department, University of Granada, where he has been an Associate Professor, since 2012. In 2017, he was an invited Visiting Professor with the KTH Royal Institute of Technology, Stockholm. He has authored more than 65 high-impact journal contributions and more than 60 contributions to international symposia. His research interests include electromagnetism and communication issues, such as radiofrequency devices, antennas, and propagation.

ÁNGEL PALOMARES-CABALLERO received the B.Sc. and M.Sc. degrees in telecommunication engineering from the University of Granada (UGR), Granada, Spain, in 2016 and 2018, respectively, and the Ph.D. degree from the Signal Theory, Telematics and Communications Department, UGR, in 2023. Currently, he is a Postdoctoral Researcher with INSA Rennes, France. His current research interests include millimeter-wave antennas, reflectarrays, and reconfigurable intelligent surfaces.

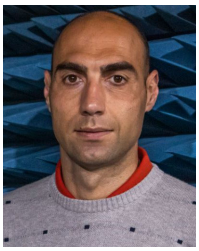

JUAN F. VALENZUELA-VALDÉS was born in Marbella, Spain. He received the degree in telecommunication engineering from Universidad de Malaga, Malaga, Spain, in 2003, and the Ph.D. degree from Universidad Politecnica de Cartagena, Cartagena, Spain, in 2008. He joined the Department of Information Technologies and Communications, Universidad Politecnica de Cartagena, in 2004. In 2007, he joined EMITE Ing., Murcia, Spain, as the Head of Research. In 2011, he joined Universidad de Extremadura, Merida, Spain. In 2015, he joined Universidad de Granada, Granada, Spain, where he is currently a Full Professor. He is also the Head of the SWAT Research Group, University of Granada, and the Co-Head of the Singular Laboratory of Electromagnetic Characterization of Microwave and Millimeter Devices and Antennas. His publication record comprised more than 100 publications, including 50 journal citation reports (JCR) indexed articles and seven book chapters. He holds several national and international patents. His current research interests include wireless communications, radio frequency devices, antennas, and propagation. He received several prizes, including the National Prize for the Best Ph.D. Thesis in mobile communications by Vodafone.

CARLOS MOLERO (Member, IEEE) was born in Seville, Spain, in April 1987. He received the Licenciado and Ph.D. degrees in physics from Universidad de Sevilla, Seville, in 2011 and 2017, respectively. From 2017 to 2020, he was a Postdoctoral Researcher with INSA Rennes, Rennes, France. Since 2020, he has been a Postdoctoral Researcher with Universidad de Granada. His research interests include the study of periodic structures, both in planar and 3-D architectures, circuit models, full-metal devices, the new conception of polarizers based on 3-D printable self-supported cells, and space–time metasurfaces. He was a recipient of some prizes, such as the Best Engineer Prize at the 2015 European Microwave Conference, Paris, France.